Acta Crystallographica Section D
Biological Crystallography
ISSN 0907-4449

The structure of a redundant enzyme: a second isoform of aspartate β-semialdehyde dehydrogenase in *Vibrio cholerae*

Ronald E. Viola,* Xuying Liu, Jeffrey F. Ohren‡ and Christopher R. Faehnle§

Department of Chemistry, The University of Toledo, Toledo, Ohio 43606, USA

‡ Current address: Pfizer Global Research and Development, Department of Structural Chemistry, Groton, CT 06340, USA.
§ Current address: Cold Spring Harbor Laboratory, Cold Spring Harbor, NY 11724, USA.

Correspondence e-mail: ron.viola@utoledo.edu

Received 12 September 2007
Accepted 27 December 2007

PDB References: *vc*ASADH2, 2qz9, r2qz9sf; *vc*ASADH2–ASA complex, 2r00, r2r00sf.

Aspartate-β-semialdehyde dehydrogenase (ASADH) is an essential enzyme that is found in bacteria, fungi and plants but not in humans. ASADH produces the first branch-point metabolite in the biosynthetic pathways that lead to the production of lysine, threonine, methionine and isoleucine as well as the cell-wall precursor diaminopimelate. As a consequence, ASADH appears to be an excellent target for the development of novel antibiotics, especially for Gram-negative bacteria that require diaminopimelate for cell-wall biosynthesis. In contrast to the Gram-negative ASADHs, which readily formed well diffracting crystals, the second isoform of aspartate-β-semialdehyde dehydrogenase from *Vibrio cholerae* (*vc*ASADH2) was less well behaved in initial crystallization trials. In order to obtain good-quality single crystals of *vc*ASADH2, a buffer-optimization protocol was used in which the initial purification buffer was exchanged into a new condition derived from a pre-crystalline hit. The unliganded structure of *vc*ASADH2 has been determined to 2.2 Å resolution to provide additional insight into the structural and functional evolution of the ASADH enzyme family. The overall fold and domain organization of this new structure is similar to the Gram-negative, Gram-positive and archeal ASADH structures determined previously, despite having less than 50% sequence identity to any of these family members. The substrate-complex structure reveals that the binding of L-aspartate-β-semialdehyde (ASA) to *vc*ASADH2 is accommodated by structural changes in the amino-acid binding site and in the helical subdomain that is involved in the dimer interface. Structural alignments show that this second isoform from Gram-negative *V. cholerae* most closely resembles the ASADH from a Gram-positive organism and is likely to bind the coenzyme in a different conformation to that observed in the other *V. cholerae* isoform.

1. Introduction

Aspartate β-semialdehyde dehydrogenase (ASADH; EC 1.2.1.11) is a highly conserved homodimeric enzyme that is involved in the conversion of β-aspartyl phosphate (βAP) to aspartate β-semialdehyde (ASA) and is found in bacteria, fungi and plants but not in mammals (Cohen, 1983; Karsten & Viola, 1991; Viola, 2001). ASADH represents the first committed step in the biosynthetic pathways that lead to the production of the essential amino acids lysine, threonine, methionine and isoleucine; it also performs a key step in the production of critical metabolic intermediates, including diaminopimelate (DAP), a required component of Gram-negative bacterial cell walls (Paidhungat *et al.*, 2000; Pavelka & Jacobs, 1996; Viola, 2001). Deletion of the *asd* gene which encodes ASADH is lethal to microorganisms, as demonstrated

by gene-knockout studies with *Legionella pneumophila* (Harb & Kwaik, 1998), *Salmonella typhimurium* (Galan *et al.*, 1990) and *Streptococcus mutans* (Cardineau & Curtiss, 1987). The combination of the critical nature of the pathway in microorganisms and its absence in humans and other mammals makes ASADH an attractive target for the development of novel antibiotics, particularly for Gram-negative bacteria (Angeles *et al.*, 1992; Viola, 2001).

Vibrio cholerae is a Gram-negative bacillus of the order γ-Proteobacteria. This organism is the causative agent of the waterborne disease cholera, which is responsible for the deaths of an estimated 120 000 individuals worldwide annually (Faruque *et al.*, 1998). *V. cholerae* contains two chromosomes, which is possibly the result of an ancient gene-capture event (Faruque *et al.*, 1998). This organism must be able to survive in the very divergent environments of an aquatic habitat and the gut of its human host and the presence of a second chromosome has been speculated to provide additional functions that help ensure its survival (Schoolnik & Yildiz, 2000). The *vc*ASADH2 isoform is found on the main chromosome along with the *vc*ASADH1 isoform and both these enzymes have significantly lower catalytic efficiency than those measured for other Gram-negative bacterial ASADHs (Moore *et al.*, 2002). Our structural and functional understanding of the ASADH enzymatic reaction has been derived from biochemical and mutational studies, as well as structural studies of the Gram-positive bacterial *Streptococcus pneumonia* ASADH (*sp*ASADH; Faehnle, Le Coq *et al.*, 2006), the Gram-negative bacterial *Escherichia coli* ASADH (*ec*ASADH; Hadfield *et al.*, 1999; Nichols *et al.*, 2004), *Haemophilus influenzae* ASADH (*hi*ASADH; Blanco, Moore & Viola, 2003; Blanco, Moore, Faehnle & Viola, 2004; Blanco, Moore, Faehnle, Coe *et al.*, 2004) and *vc*ASADH1 (Blanco, Moore, Kalabeeswaran *et al.*, 2003) and the hyperthermophilic archeal *Methanococcus jannaschii* ASADH (*mj*ASADH; Faehnle *et al.*, 2005). The ASADH catalytic mechanism is initiated by an active-site cysteine thiolate formed through proton abstraction by a histidine base. This cysteine nucleophile carries out a nucleophilic attack on the carbonyl of the L-β-aspartyl phosphate substrate to form a tetrahedral thioacyl intermediate. Expulsion of inorganic phosphate leads to the formation of a covalently bound acyl-enzyme intermediate. Reduction of the acyl-enzyme intermediate as a result of a hydride transfer from NADPH produces a second tetrahedral intermediate, the collapse of which leads to the release of the ASA product and regeneration of the catalytic residues (Blanco, Moore, Kalabeeswaran *et al.*, 2003).

Inhibitors of ASADH include thiol-specific reagents in general, as well as substrate-analogue thiols such as *S*-methylcysteine sulfoxide (SMCS), which forms a covalent disulfide bond with the catalytic cysteine to inactivate the enzyme (Karsten & Viola, 1992). Oxyanions are weak competitive inhibitors of ASADH activity that compete directly with phosphate binding. Periodate is the most potent of the oxyanions, with an estimated K_i of 0.22 m*M* (Kish & Viola, 1999). The most drug-like inhibitor of ASADH reported to date is a difluorophosphonate analog of aspartyl phosphate, with a K_i of 95 μM (Cox *et al.*, 2001; Han *et al.*, 2003). Interestingly, while the residues involved in substrate binding and catalysis are highly conserved for all the ASADH enzymes, their catalytic activity and the degree of subunit association and interdomain communication are not. Structures of the open and closed forms of the Gram-negative ASADH enzymes have provided a rationale for subunit communication across the functional homodimer interface and a structural basis for the observed half-of-sites reactivity (Blanco, Moore, Kalabeeswaran *et al.*, 2003; Nichols *et al.*, 2004). The recently determined structure of *sp*ASADH demonstrated that the intersubunit communication channel remains highly conserved in both Gram-negative and Gram-positive bacteria (Faehnle, Le Coq *et al.*, 2006). However, the catalytic activity of this Gram-positive ASADH is significantly lower than those of the Gram-negative ASADHs. The hyperthermophilic *mj*ASADH structure also displayed a significantly reduced catalytic activity and additionally the structure showed a complete loss of the intersubunit communication channel found in all previously determined ASADH structures (Faehnle *et al.*, 2005). The reduction in catalytic activity found in *mj*ASADH and *sp*ASADH also seems to correlate with a significant reduction in subunit contact area, suggesting a role for the quaternary structure of ASADH in its enzymatic efficiency.

Here, we report the first structure of *vc*ASADH2 and show that this isoform is quite different from the *vc*ASADH1 isoform and in fact more closely resembles the Gram-positive *sp*ASADH structure. Crystallization was accomplished by buffer optimization and the structural and functional differences between these *V. cholerae* isoforms were assessed. Novel anti-cholera drugs designed to target the aspartate pathway are feasible, but intervention at this step in the pathway will require compounds that inhibit both isoforms of ASADH.

2. Experimental procedures

2.1. Enzyme purification, kinetics and crystallization

The *vc*ASADH2 used in this study was cloned, recombinantly expressed in *E. coli* and purified to greater than 95% purity using anion-exchange and size-exclusion chromatography (Moore *et al.*, 2002). The initial protein-storage buffer was chosen as 100 m*M* Tris–HCl buffer pH 8.5 with 500 m*M* KCl based on optimal enzymatic activity. While the protein was highly pure and quite active in the initial protein-storage buffer, dynamic light-scattering experiments showed that the protein was polydisperse with the presence of higher molecular-weight aggregates (data not shown). The protein sample was screened for crystallizability against a standard panel of sparse-matrix conditions (Crystal Screens I and II, Hampton Research, Aliso Viejo, California, USA) at both room temperature and 286 K at a protein concentration of 10 mg ml^{-1}. Poorly formed pre-crystalline aggregates were found to grow very rapidly from a few of the lower pH crystallization conditions, while most conditions produced heavy

precipitate. Extensive grid screening around the variables of pH, ionic strength and precipitant concentration identified from the most likely condition (50 m*M* sodium citrate pH 5.6, 30% PEG 4000 and 0.2 *M* ammonium acetate) led to single crystals, which tended to be small and poorly ordered (Fig. 1*a*). Further screening of the protein in the original buffer did not produce diffraction-quality crystals. Dynamic light-scattering studies showed that this protein was highly aggregated. We hypothesize that a component in the optimized crystallization conditions helped to stabilize the formation of a crystalline lattice, since no other conditions from the sparse-matrix screens produced diffraction-quality crystals.

In order to determine whether the crystallization was being driven by a decrease in pH or by the addition of the polyethylene glycol, the purified protein was dialyzed from the Tris-based storage buffer into 50 m*M* sodium citrate pH 5.6 with 0.2 *M* ammonium acetate and 2 m*M* DTT, *i.e.* conditions similar to those found in the initial crystallization hits without the inclusion of the polyethylene glycol precipitant (Schubert *et al.*, 2001). After overnight dialysis at 277 K, a fine white precipitate was observed that redissolved on increasing the concentration of Tris buffer to 100 m*M* in the absence of KCl. The remaining sample was then diluted back into 100 m*M* Tris buffer pH 8.5 with 200 m*M* ammonium acetate instead of KCl and 5 m*M* DTT before being concentrated to 12 mg ml^{-1}. Diffraction-quality single crystals were obtained by screening against a three-dimensional grid of 50–200 m*M* sodium citrate buffer from pH 5.2 to pH 6.4 *versus* 0.1–0.4 *M* ammonium acetate over the range 14–28% PEG 8000 with a fixed concentration of 2 m*M* DTT (Fig. 1*b*).

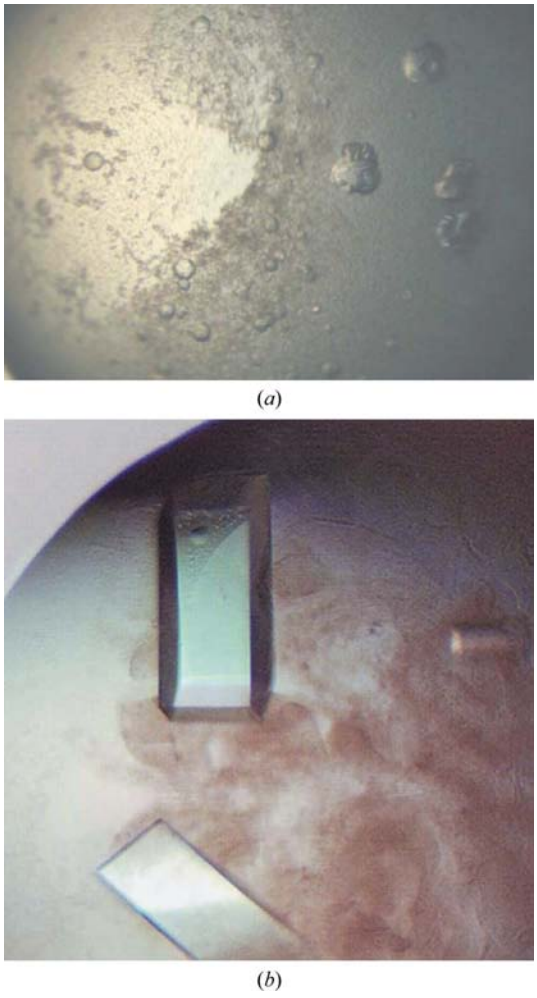

Figure 1
Crystallization of *vc*ASADH2. (*a*) Pre-crystalline aggregates obtained in 50 m*M* citrate pH 5.5, 30% PEG 4000 and 200 m*M* ammonium acetate. (*b*) Crystals obtained after dialysis into 100 m*M* Tris pH 8.5 and 200 m*M* ammonium acetate.

Large single crystals were grown at 293 K (Fig. 1*b*) using the hanging-drop vapor-diffusion method from 1 µl droplets of 12 mg ml^{-1} protein solution added to a 1 µl drop of well solution suspended over a 600 µl reservoir containing 24–27% PEG 8000 with 0.2–0.4 *M* ammonium acetate and 5 m*M* DTT using 0.1 *M* sodium citrate buffer in the pH range 5.5–6.5. Crystals suitable for X-ray analysis with dimensions of 0.1–0.3 mm grew in 3–4 d. The crystallization of *vc*ASADH2 was found to be highly dependent on the final protein concentration, with an optimal concentration of ∼12 mg ml^{-1}. No crystals were obtained at protein concentrations below 10 mg ml^{-1} and poorly formed aggregates grew at concentrations greater than 12 mg ml^{-1}. The effect of ionic strength and pH were found to offset each other, with the lower pH condition (pH 5.5) requiring higher concentrations of ammonium acetate (∼0.4 *M*), while the pH 6.0 condition only crystallized well with 0.2 *M* ammonium acetate. Ammonium acetate concentration was varied from 0.15 to 0.4 *M*, while sodium citrate was optimal over a very narrow range of ∼75–100 m*M*. PEG 8000 concentrations in the range 21–30% were found to be effective, with the best condition between 24 and 27% PEG 8000. Lower molecular-weight PEGs from PEG 1000 to PEG 4000 also gave single crystals, but these were of lower diffraction quality.

2.2. Crystal soaking, cryoprotection and X-ray data collection

The crystals were prepared for soaking experiments and low-temperature data collection by using a cryoloop to transfer a crystal grown using 27% PEG 8000, 300 m*M* ammonium acetate, 5 m*M* DTT and 100 m*M* sodium citrate pH 5.5 from the mother-liquor solution into 10 µl of an artificial mother liquor (AML) solution for long-term storage. The AML solution was made by adding 100 µl 1.0 *M* sodium citrate pH 5.5, 200 µl 2.0 *M* ammonium acetate, 240 µl 50% PEG 8000 and 60 µl dH_2O to an Eppendorf tube (final concentrations 167 m*M* citrate, 667 m*M* acetate and 20% PEG 8000). A 1:10 dilution of ASA was made by adding 20 µl 80 m*M* ASA to a final concentration of 100 m*M* Tris pH 8.5 in dH_2O. 2 µl of the ASA solution was then added to the 10 µl AML drop containing the crystal and allowed to soak for 20 min at room temperature. A cryoprotected AML (cAML) solution was made by adding 10 µl of a 100% ethylene glycol (EG) solution to 90 µl of the AML solution. 1 µl of the cAML solution was placed on the cover slip adjacent to the crystal in the ASA/AML drop and mixed with 1 µl of the ASA/AML solution to create an ASA/cAML solution containing 5% EG

Table 1
Crystallographic data-collection and refinement statistics.

Values in parentheses are for the highest resolution shell.

	Apo enzyme	ASA complex
Data collection		
Space group	*C*2	*C*2
Unit-cell parameters (Å, °)	a = 119.3, b = 85.7, c = 116.1, α = 90, β = 103.7, γ = 90	a = 122.4, b = 84.7, c = 115.0, α = 90, β = 102.1, γ = 90
Resolution (Å)	40–2.2 (2.26–2.20)	40–2.0 (2.08–2.03)
Redundancy	4.1 (4)	3.6 (4)
Completeness (%)	99.6 (94.3)	99.7 (96.1)
$R_{\rm merge}$† (%)	4.9 (40.0)	5.3 (33.0)
$I/\sigma(I)$	23 (3)	27 (5)
Refinement statistics		
Resolution range (Å)	40–2.2	40–2.0
Wilson B factor (Å^2)	36.8	31.8
No. of reflections	57268	73968
$R_{\rm cryst}/R_{\rm free}$ (%)‡	19.6/24.5	18.5/22.9
R.m.s.d. bonds (Å)	0.010	0.011
R.m.s.d. angles (°)	1.24	1.22
No. of molecules per ASU	3	3
No. of atoms		
Protein	7809	7404
Ligand	0	8
Water	406	767
B factors (Å^2)		
Protein	41.1	29.5
Ligand	—	25.6
Water	47.0	43.1
Ramachandran plot analysis§ (%)		
Most favored	90.9	92.3
Additionally allowed	7.5	8.3
Generously allowed	0.6	0.2
Disallowed	0	0

† $R_{\rm merge} = \sum_{hkl}\sum_i |I_i(hkl) - \langle I(hkl)\rangle| / \sum_{hkl}\sum_i I_i(hkl)$, where $I_i(hkl)$ is the intensity of an individual measurement and $\langle I(hkl)\rangle$ is the mean intensity of this reflection. ‡ $R_{\rm cryst} = \sum |F_{\rm o} - F_{\rm c}| / \sum |F_{\rm o}|$, where $|F_{\rm o}|$ and $|F_{\rm c}|$ are the observed and calculated structure-factor amplitudes, respectively. $R_{\rm free}$ is the cross-validation R value calculated for 5% of the reflections omitted from the refinement. § Analysis of the Ramachandran plots was performed with the program *PROCHECK* (Laskowski *et al.*, 1993).

as a cryoprotectant. The crystal was transferred to the cryo-protected ASA/cAML solution and allowed to equilibrate for 10 min. After equilibration, the crystal was removed from the ASA/cAML solution and transferred into ∼2 µl of a mixture of 30% mineral oil and 70% Paratone-N oil (cryo-oil) using a mounted cryoloop. The crystal was carefully passed through the cryo-oil drop so that the crystal was completely bathed in the oil and to ensure that all the aqueous solvent was removed. Finally, the crystal was flash-cooled by direct immersion into liquid nitrogen.

Synchrotron X-ray diffraction data for apo *vc*ASADH2 were collected on an ADSC Quantum 210 CCD detector at a wavelength of 1.00 Å at 100 K on the Industrial Macromolecular Crystallography Association (IMCA) beamline 17-ID at the Advanced Photon Source, Argonne National Laboratory. Synchrotron X-ray diffraction data for the ASA complex of *vc*ASADH2 were collected on an ADSC Quantum IV CCD detector at a wavelength of 0.90 Å at 100 K on the BioCARS beamline 14-BM-C at the Advanced Photon Source, Argonne National Laboratory. Diffraction data for both data sets were processed using *DENZO* and *SCALEPACK* from the *HKL*-2000 program suite (Otwinowski & Minor, 1997). The space group was determined to be centered monoclinic *C*2 with three molecules per asymmetric unit, corresponding to a solvent content of approximately 53% (Matthews, 1974).

2.3. Structure determination and refinement

The structure of the ASA complex of *vc*ASADH2 was solved by the molecular-replacement method with the program *Phaser* (McCoy *et al.*, 2005) using a search model consisting of a single monomer of *mj*ASADH (PDB code 1ys4) with the nonhomologous regions removed (Faehnle *et al.*, 2005). The structure of the unliganded form of *vc*ASADH2 was solved by molecular replacement with the program *MOLREP* (Vagin & Teplyakov, 1997) from the *CCP*4 suite (Collaborative Computational Project, Number 4, 1994) using a single monomer of *vc*ASADH2 as the search model. Structural refinement calculations and electron-density maps were calculated with the program *REFMAC*5 (Murshudov *et al.*, 1997) from the *CCP*4 suite using the complete data with no resolution or σ cutoff. Manual fitting and real-space refinement of the protein model were performed with the program *QUANTA*-2000 (Accelrys Inc., San Diego, California, USA). The asymmetric unit of both of the *vc*ASADH2 structures contains three monomers, of which two are found to form an ASADH homodimer while the third forms a homodimer with a symmetry-related monomer in the adjacent asymmetric unit. The final data-collection and crystallographic refinement statistics are summarized in Table 1.

2.4. Structural analysis

Structural analysis and preparation of figures were performed with an internal molecular-viewing program (J. Moon *et al.*, unpublished program). Additional structural analysis was performed using the web-based interface for *DynDom* located at http://www.sys.uea.ac.uk/dyndom (Hayward & Berendsen, 1998). Sequence-based alignments were generated using the *ClustalW* web-based server (Lassmann & Sonnhammer, 2006) located at the European Bioinformatics Institute (http://www.ebi.ac.uk/clustalw). Structural-based alignments were performed using the *TOPP* program (Lu, 1996) through the *CCP*4 interface and the web-based interface for *ESPript* v.2.2 located at http://espript.ibcp.fr/ESPript/ESPript (Gouet *et al.*, 1999). Coordinate files containing the percentage identity among ASADH-family members were created by transferring the numerical values representing the degree of conservation derived from the *ClustalW* alignment of representative ASADH orthologs into the *B*-factor column of the unliganded *vc*ASADH2 chain *A*. Surface-area calculations were performed using *Surface Racer* v.4.0 (Tsodikov *et al.*, 2002) with a solvent probe radius of 1.4 Å.

3. Results and discussion

3.1. Crystallization of *vc*ASADH2 through optimization of the initial conditions

The identification of well diffracting crystals continues to be a critical bottleneck in the structure determination of macro-

molecules. There are two complementary approaches for obtaining the 'best' diffraction-quality crystals of a particular protein. The most widely used method is the identification of an initial crystalline hit derived either from a focused library design (Anderson *et al.*, 2006; Kantardjieff & Rupp, 2004; Kimber *et al.*, 2003) or from a sparse-matrix approach (Chayen & Saridakis, 2002; Jancarik & Kim, 1991; Newman *et al.*, 2005) followed by optimization of the final crystallization conditions (Carter, 1997; Carter & Carter, 1979; Cudney *et al.*, 1994; Tran *et al.*, 2004). Alternatively, optimization of the starting components can also lead to improved crystal quality of the final product. The former approach has been very effective, producing crystals that have led to many of the increasing number of structures deposited in the PDB. However, the latter approach has become a recognized tool for handling the large number of difficult protein samples that did not produce usable crystals after initial screening.

Thus, two schools of thought have emerged for selecting the optimal protein buffer for crystallization: the use of a screening strategy to optimize protein solubility prior to crystallization (Collins *et al.*, 2004; Izaac *et al.*, 2006; Jancarik *et al.*, 2004) or the use of the initial round of crystallization as a tool to iteratively guide the optimization of the protein buffer (Collins *et al.*, 2005; Faehnle, Liu *et al.*, 2006; Schubert *et al.*, 2001). In contrast to the 'optimum solubility' approach, in which buffer conditions which produce highly soluble protein solutions are selected, successful crystallization has been achieved by following the strategy of selecting an improved initial buffer composition based on the ability to support formation of pre-crystalline material from the initial crystallization screen (Faehnle, Le Coq *et al.*, 2006; Schubert *et al.*, 2001). In a sense, this approach is similar to the 'reverse-screening' strategy (Stura *et al.*, 1994), in which small-scale precipitation studies are conducted to guide the choice of protein buffer and ultimately the precipitant component system. With this approach, the identification of pre-crystalline material (Fig. 1*a*) in an initial round of screening was used as a guide to select the appropriate protein buffer and precipitant. The reduction in the KCl concentration in the optimized protein buffer is one of the likely reasons for the improvement in the crystallization of *vc*ASADH2. KCl has a stronger precipitating effect compared with ammonium acetate, so exchanging these two salts helped to keep the protein in solution and allowed it to slowly precipitate as well formed crystals.

Crystallization of this protein from *V. cholerae* had been attempted for several years without success prior to using the buffer-exchange protocol. However, another ASADH ortholog from *S. pneumoniae* was recently crystallized using this same approach (Faehnle, Le Coq *et al.*, 2006). A full multivariant analysis of the protein buffer was not performed; however, this solution was optimized through the addition of the components from the initial crystallization hit and a reduction in the amount of KCl. This idea of using the initial screening hit as a method for identifying the components of a new protein buffer solution has only been explicitly described in a few instances (Faehnle, Le Coq *et al.*, 2006; Schubert *et al.*, 2001). This approach ultimately produced crystals of *vc*ASADH2 diffracting to ∼2.0 Å resolution that were used in this study (Fig. 1*b*).

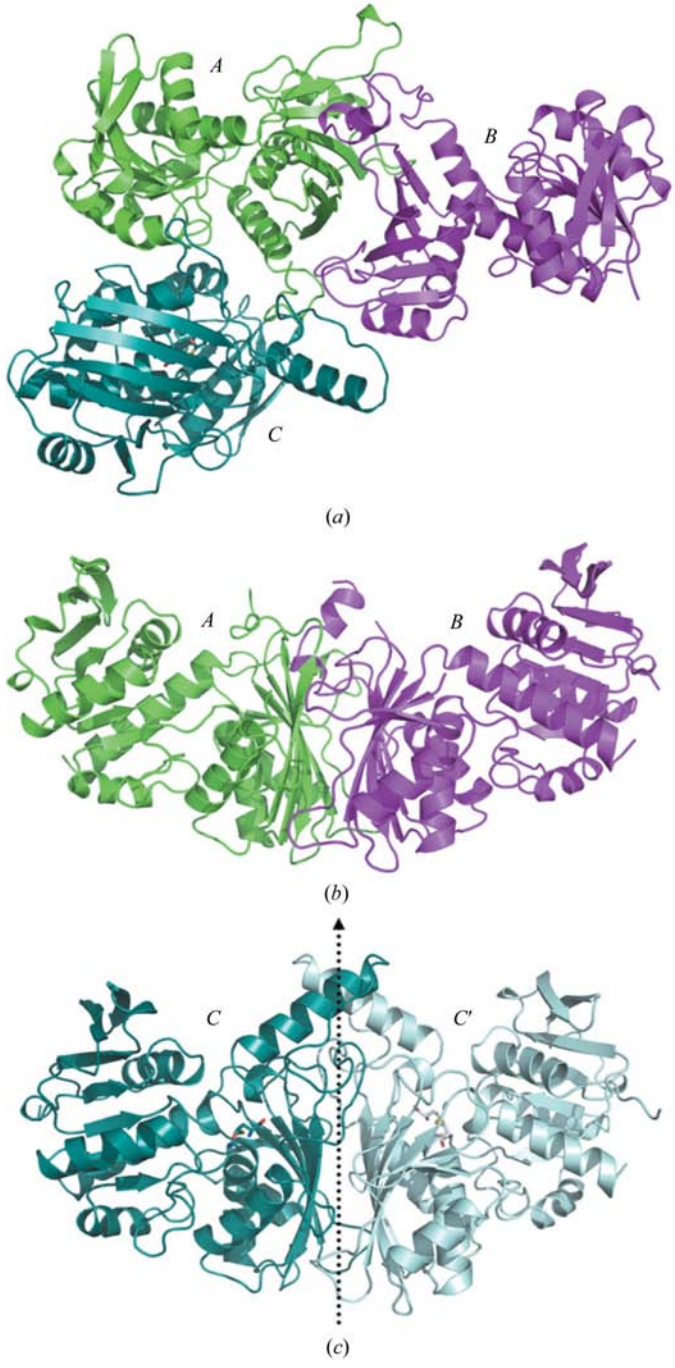

Figure 2
V. cholerae ASADH2 assembles with the typical ASADH folding. (*a*) The top view of the quaternary structure in the asymmetric unit. Monomers *A* and *B* form a dimer within the asymmetric unit, while the second dimer is formed by monomer *C* and the symmetry-related monomer. (*b*) A side view of the dimer formed by monomers *A* and *B*. ASA is not bound in this dimer and the α-helical subdomains are disordered. (*c*) A side view of the homodimer formed by monomer *C* and the symmetry-related monomer *C*′. The dotted arrow represents the twofold crystallographic symmetry axis and ASA is covalently bound in this dimer.

3.2. Structure determination and analysis

Just as the crystallization of *vc*ASADH2 required an alternative approach to produce well diffracting crystals, the structure determination was also somewhat challenging. While the homodimer interface is highly conserved among the ASADH orthologs, subtle differences in monomer orientation and conformation, combined with the presence of three molecules in the asymmetric unit, precluded successful phase determination by the molecular-replacement (MR) method using each of the earlier Gram-negative ASADH structures (including the other *V. cholerae* ASADH isoform) as search models. Only after the more homologous *mj*ASADH structure had been determined by selenomethione MAD phasing (Faehnle *et al.*, 2005) was an effective search model available; this was created by truncation of the nonconserved structural elements. The refined *vc*ASADH2 structure revealed one of the problems that was encountered during the initial MR attempts. There are two different but related homodimers that can be created from the three molecules in the asymmetric unit. The first is formed by two closely related monomers within the asymmetric unit (Fig. 2*a*; monomers *A* and *B*), while a second homodimer is created by symmetry with a monomer (Fig. 2*a*; monomer *C*) from an adjacent unit cell. In addition, subsequent comparisons of the refined model of *vc*ASADH2 showed r.m.s. differences of 1.6–1.7 Å from the other Gram-negative ASADHs (Table 2) that would made MR starting from these search models challenging.

Figure 3
Domain movement caused by ASA binding in *vc*ASADH2. The binding of ASA to the active site induces a 5° rotation of the α-helical dimerization subdomain towards the N-terminal domain. ASA, shown in stick representation, is covalently bound to Cys133. The fixed domain, the hinge-bending residues and the moved subdomain in the apo enzyme are colored blue, green and red, respectively. The complex structure is colored yellow and superimposed on the apo structure. The axis of domain movement is represented as a black dotted line.

Table 2
ASADH structure and activity comparisons.

Enzyme form	Sequence identity to *vc*ASADH2 (%)	Buried dimer surface (Å^2)	Percentage of total surface buried	R.m.s.d. to *vc*ASADH2 dimer (Å)	k_{cat}† (s^{-1})
*ec*ASADH‡	26	3834	23	1.6	610
*vc*ASADH1	27	3620	22	1.7	120
*hi*ASADH	27	3478	21	1.6	330
*sp*ASADH	49	2673	17	1.0	2
*vc*ASADH2	—	2351	16	—	58
*mj*ASADH	38	1943	13	1.3	4§

† Data taken from Moore *et al.* (2002) and from Faehnle, Le Coq *et al.* (2006) for *sp*ASADH. ‡ *ec*, *E. coli*; *vc*, *V. cholerae*; *hi*, *H. influenzae*; *sp*, *S. pneumonia*; *mj*, *M. jannaschii*. § Measured at 343 K.

The *vc*ASADH2 structure determined in this study retains the overall domain organization and conserved hydrophobic β-sheet interface that forms the functional homodimer that is the likely physiological species for all ASADHs (Faehnle *et al.*, 2005). The two molecules that make up the complete apo homodimer are nearly identical, with an average backbone root-mean-square deviation (r.m.s.d.) after superposition of only 0.24 Å. Each of the monomers consists of two domains: the amino-terminal coenzyme-binding domain (β1–β6, α1–α5, α11) containing a classical Rossmann-fold motif responsible for binding the NADP cofactor and a carboxyl-terminal catalytic and dimerization domain (β7–β14, α6–α10) in which the catalytic site and the homodimer interface are located.

Soaking of ASADH apo crystals with the substrate aspartate-β-semialdehyde (ASA) has been shown to allow the formation of an acyl-enzyme intermediate without changing the overall assembly of the dimeric structure (Faehnle, Le Coq *et al.*, 2006). However, no ASA density is observed in the functional dimer formed by monomers *A* and *B* (Fig. 2*b*) when these crystals are soaked with the substrate. Unexpectedly, the helical interface subdomain of monomers *A* and *B* becomes disordered in this structure (Fig. 2*b*), resulting in an exposed substrate-binding site. However, density is observed for ASA in monomer *C*, which forms a symmetry-related dimer with a monomer from the adjacent asymmetric unit (Fig. 2*c*). This ASA is trapped in the active site as an acyl intermediate through a covalent bond to the active-site nucleophile, Cys133, while the active-site residues Glu214 and His246 maintain essentially the same orientation and position as in the apoenzyme structure. The C$^{\alpha}$ position of the substrate-binding residue Arg239 moves towards the bound ASA by 0.4 Å as a result of a helical subdomain movement (Fig. 3). This movement causes the guanido N atoms to shift by 0.9 Å into the position required to form a bidentate interaction with the substrate carboxyl group.

There is also some unexpected density found in the active site of monomer *C* adjacent to the bound substrate. This density does not correspond to any of the components present in the crystallization buffer and is best fitted as a molecule of oxalate that is proposed to arise as one of the breakdown

products of polyethylene glycol solutions as they age (Ellis, 2006; Kryuk *et al.*, 2002).

To investigate the domain movements induced by substrate binding, the *DynDom* program (Hayward & Lee, 2002) was used to identify the mobile regions and to identify the hinge-bending residues that allow this domain movement. The fixed region is predominately composed of residues from the N-terminal cofactor-binding domain and the lower portion of the C-terminal dimerization domain. The mobile region contains the upper portion of the C-terminal dimerization domain, including the helical subdomain and the loops connected to the interface β-sheet. The binding of ASA causes a relatively modest 5° rotation toward the C-terminal domain around a hinge axis (Fig. 3). The hinge-bending regions along this axis consists of the following set of residues, with the amino acid in the mobile region listed first: Asn156-Val157, Cys199-Asn198, Val238-Arg239 and His246-Gly245 (highlighted in green in Fig. 3). Two of the amino-acid residues in these bending regions, Arg239 and His246, are directly involved in ASA binding. The remainder of the backbone that makes up the active-site cleft of *vc*ASADH2 is unchanged upon substrate binding.

3.3. Sequence and structural comparison of the ASADH orthologs

The ASADH family has been subdivided into three structural branches consisting of the enzymes from Gram-negative bacteria, from Gram-positive bacteria and from archaea/fungi. However, some Gram-negative bacteria such as *V. cholerae* (the causative agent of the deadly intestinal disease cholera) and *Legionella pneumophila* (one of the causative agents of Legionnaires' disease) have two chromosomes and as such have two copies of many genes, including the *asd* gene that codes for ASADH. The structure of the first isoform of ASADH from *V. cholerae* (*vc*ASADH1) was found to be highly homologous to the previously determined structure of *ec*ASADH, a result that was predicted from their high sequence identity. Together with the structure of *hi*ASADH,

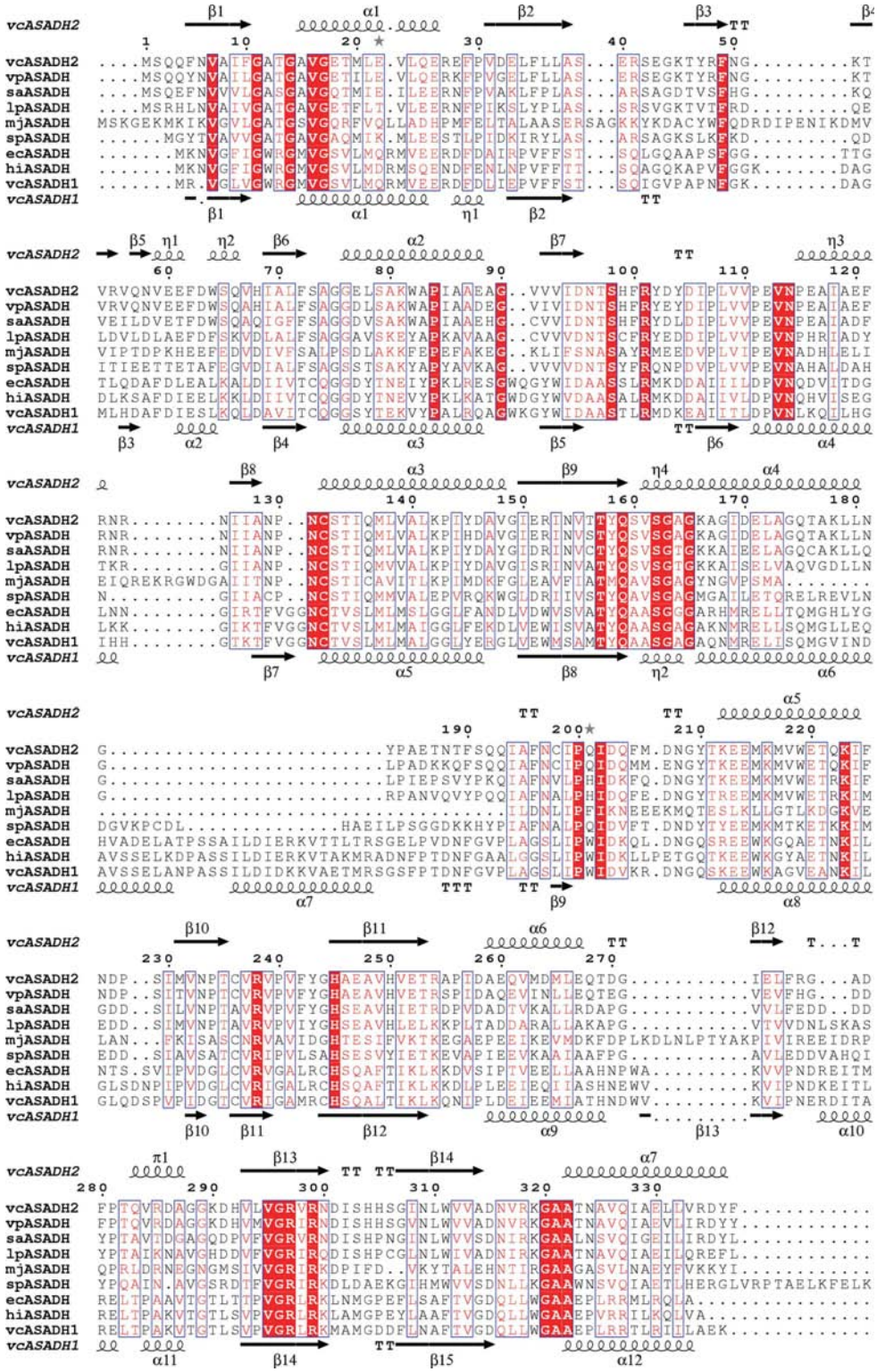

Figure 4
Sequence alignment among representative members of the ASADH family.

these three ASADH orthologs make up the 'classical' Gram-negative family of ASADH structures.

A sequence and structural alignment among representative bacterial and archaeal ASADHs (Fig. 4) reveals only 31 amino-acid residues (~9%) that are strictly conserved out of the 338 residues in *vc*ASADH2. Despite the low level of sequence identity, *vc*ASADH2 retains the same overall domain organization and the same set of key active-site functional groups and therefore the same catalytic mechanism as the other ASADH-family members. The percentage identity determined by the sequence and structural alignment was mapped onto the surface of the *vc*ASADH2 homodimer structure. This map illustrates that the most highly conserved residues found among the ASADH-ortholog structures are clustered within the active-site cavity and include those groups involved in substrate binding and catalysis (Fig. 5). In addition, the communication channel that links the two active sites across the homodimer interface that was first observed in the *vc*ASADH1 structure (Blanco, Moore, Kalabeeswaran *et al.*, 2003) is conserved among all of the ASADH-family members that have been structurally characterized, with the exception of the archeal *mj*ASADH.

There are also differences among the various ASADHs at the dimer interface that correlate with their differences in catalytic activity. The enzyme from *E. coli* has the highest catalytic activity of the ASADHs that have been kinetically characterized and also has the largest buried dimer surface area (Table 2). The other structurally characterized ASADHs from Gram-negative bacteria have lower k_{cat} values and small dimer interface areas, while the archaeal ASADH has a dimer contact surface that is only half that of *ec*ASADH and this enzyme form also has the lowest catalytic efficiency. ASADH isoform 2 from *V. cholerae* has significantly less buried dimer surface area than isoform 1 and possesses only half of the catalytic activity (Table 2). Enzymes such as ASADH that show cooperativity between their catalytic units can be more responsive to changes in their environment. It appears that at least for this family of enzymes, the improved cooperativity that can potentially be derived from greater surface contacts between adjacent subunits can also lead to improved overall catalytic efficiency.

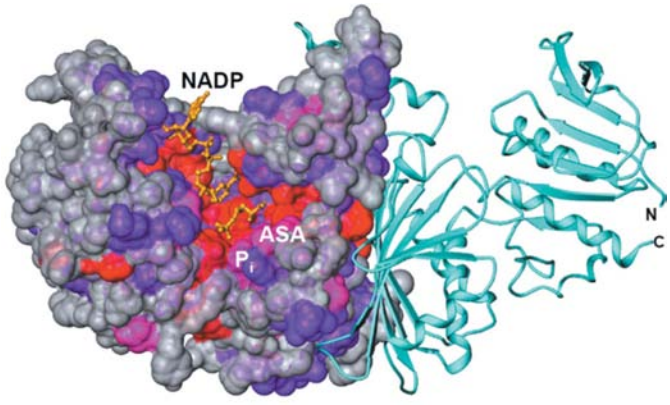

Figure 5
A map of the surface of *vc*ASADH2 color-coded to show the location of the conserved residues in the ASADH enzyme family. Red, >90% conserved; pink, 81–90% conserved; purple, 61–80% conserved; gray, nonconserved (<60%).

3.4. Sequence and catalytic activity comparisons of the *V. cholerae* ASADH isoforms

This second ASADH isoform, *vc*ASADH2, present in the Gram-negative bacterium *V. cholerae* is composed of an amino-acid sequence that is more closely related to that of the Gram-positive *sp*ASADH than it is to that of the other ASADH isoform present in this organism, *vc*ASADH1. Even more surprisingly, both *sp*ASADH and *vc*ASADH2 are more structurally similar to the hyperthermophilic archeal *M. jannaschii* ASADH (*mj*ASADH) than they are to the Gram-negative ASADHs (Table 2).

The two isoforms of ASADH present in *V. cholerae* have only 27% sequence identity and the surface area of the dimer interface in isoform 2 is only 65% that of isoform 1 (Table 2). Both *V. cholerae* ASADHs have relatively low catalytic efficiency when compared with the other Gram-negative enzymes, with the k_{cat} for *vc*ASADH1 being only 20% that of the *E. coli* ASADH, while that for isoform 2 is only 10% of the *E. coli* ASADH k_{cat} value (Moore *et al.*, 2002). The low activity of the *V. cholerae* forms of ASADH may explain the need to utilize a second isoform of the enzyme that can allow increased flux through the aspartate pathway. While the substrate K_m values are comparable among the Gram-negative ASADHs, the K_m value for phosphate is 20-fold higher in *vc*ASADH2 compared with *vc*ASADH1 (Moore *et al.*, 2002). A differential response to phosphate levels between these two isoforms would provide reserve capacity to increase

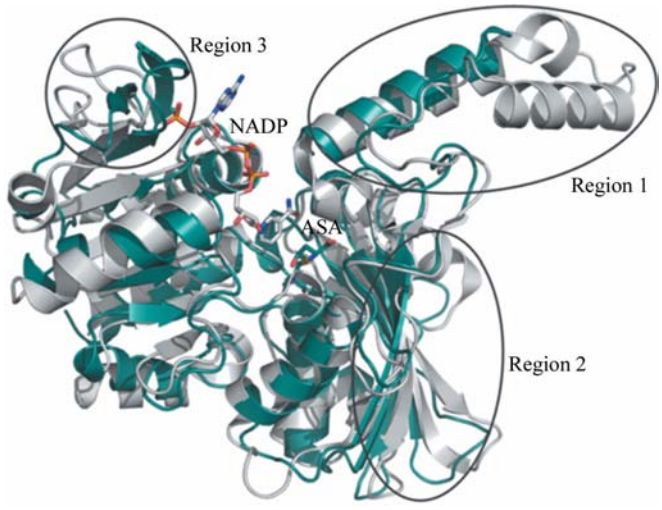

Figure 6
Structural comparison of the *V. cholerae* ASADH isoforms. In region 1 *vc*ASADH2 (blue) has a shorter α-helical subdomain with the deletion of 27 residues compared with this subdomain in *vc*ASADH1 (white). There are fewer β-sheet segments in the subunit interface in *vc*ASADH2 (region 2) and the long flexible NADP-binding loop in *vc*ASADH1 is replaced by two stable β-strands in *vc*ASADH2 (region 3). The NADP in *vc*ASADH1 is is shown in a white stick representation and ASA in *vc*ASADH2 is shown as teal sticks.

the production of essential amino acids during periods of high protein synthesis or low phosphate availability.

3.5. Structural comparison of the *V. cholerae* ASADH isoforms

In addition to the differences in sequence and catalytic efficiency, the two ASADH isoforms found in *V. cholerae* also show some significant structural differences. Both enzymes assemble into the typical ASADH fold with the N-terminal Rossmann fold and C-terminal dimerization domain that have been found throughout the ASADH family. The larger dimer interface found in *vc*ASADH1 is formed by a hydrophobic

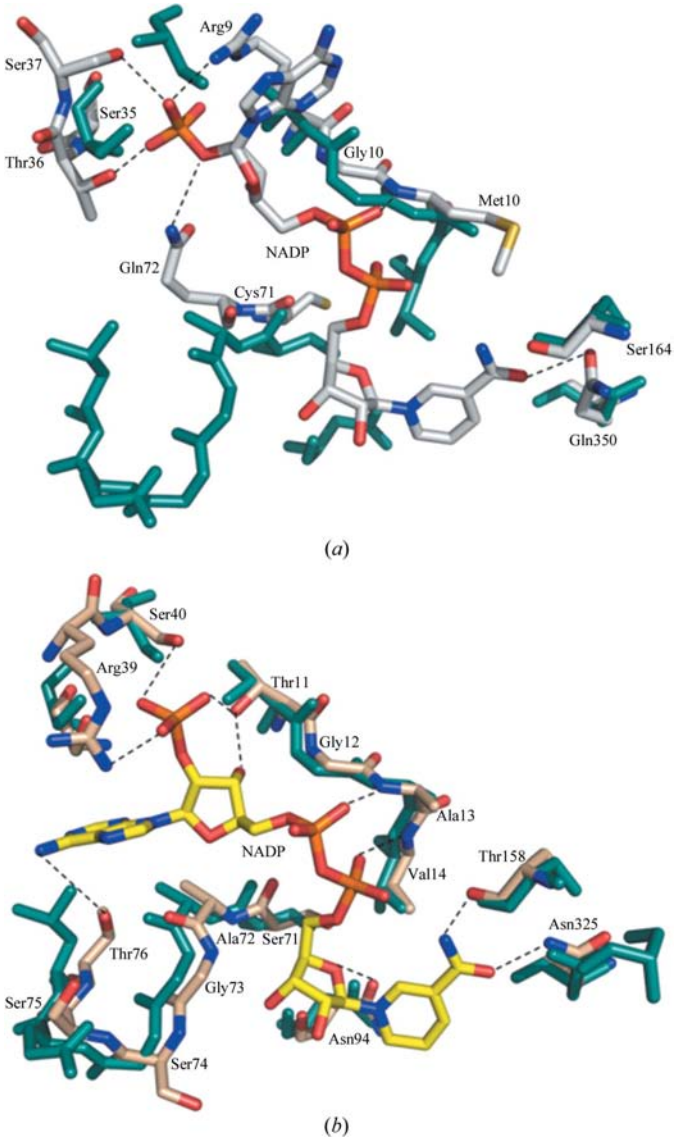

Figure 7
The NADP cofactor-binding sites in ASADHs. (*a*) There are significant differences in the NADP-binding pocket between the residues in *vc*ASADH1 (white) and those in *vc*ASADH2 (blue). (*b*) In contrast, the residues of *sp*ASADH (pink) align quite well with those of *vc*ASADH2 (blue), suggesting a similar NADP-binding orientation. Dashed lines indicate the hydrogen bonds between NADP and binding residues within 3.5 Å.

β-sheet and a helical subdomain that together contribute over 3600 Å^2 of buried surface area. The most striking difference in this region in *vc*ASADH2 is a 27-residue deletion in the single α-helix subdomain which forms the top portion of the dimer interface (Fig. 6, region 1). This truncation, along with the presence of fewer β-sheet segments in the subunit interface (Fig. 6, region 2), leads to a decrease of about 1300 Å^2 in buried surface area between the two monomers (Table 2). While there is a clear trend towards lower activity for the enzyme forms with smaller dimer interfaces, there is certainly not a linear correlation. Other factors, including the number and the types of intersubunit interactions, will undoubtedly also play a significant role.

Structural differences between two isoforms are also observed in the NADP-binding site. *vc*ASADH1 has a large and flexible coenzyme-binding loop which is conserved in the Gram-negative ASADHs (Blanco, Moore, Kalabeeswaran *et al.*, 2003). While *vc*ASADH2 has the same number of amino-acid residues in this region as *vc*ASADH1, this flexible loop is replaced in *vc*ASADH2 by two stable β-strands (Fig. 6, region 3), resulting in a more highly constrained NADP-binding pocket. The residues involved in NADP binding in *vc*ASADH2 are nearly identical to those found in the Gram-positive *sp*ASADH rather than those found in its isoform *vc*ASADH1 (Fig. 7*a*). This is consistent with the higher homology observed between *sp*ASADH and *vc*ASADH2. While *vc*ASDH1 binds NADP in the typical Gram-negative cofactor-binding pocket (Fig. 7*b*), NADP will most likely bind to *vc*ASADH2 in the altered conformation previously observed in Gram-positive ASADHs.

4. Conclusions

The conserved nature of the amino-acid-binding site of the ASADHs suggests a starting point for a structure-guided approach to the design of targeted inhibitors for use as broad-spectrum antimicrobials. While the overall fold and domain organization of *vc*ASADH2 are similar to those of other previously determined ASADH structures, the structure is more closely related to the archeal *mj*ASADH and Gram-positive *sp*ASADH structures than it is to the Gram-negative *ec*ASADH and *hi*ASADH structures. There are also significant structural differences between the two isoforms of ASADH found in *V. cholerae*. The helical interface subdomain of *vc*ASADH2 is not only involved in stabilizing the dimer interactions in this enzyme but also plays a role in coenzyme binding. The different binding pockets for the adenine moiety of NADP between the Gram-negative and Gram-positive forms of the enzyme may allow the development of inhibitors with differential affinity for these two ASADH families.

We thank Dr Roger Moore (Rocky Mountains Laboratories) for the initial cloning and purification of *vc*ASADH2, Dr Chris Whitehead for his thoughtful review of the manuscript and the staff at both IMCA-CAT and BioCARS for their

assistance with the synchrotron data collection. We also thank Drs Jim Pflugrath and Alex McPherson for instructions on the use of cryo-oil for low-temperature data collection. Use of the Advanced Photon Source was supported by the US Department of Energy, Basic Energy Sciences, Office of Science under Contract No. W-31-109-Eng-38. Access to the IMCA-CAT facilities are supported by the companies of the Industrial Macromolecular Crystallography Association through a contract with Illinois Institute of Technology (IIT), executed through IIT's Center for Synchrotron Radiation Research and Instrumentation. Use of BioCARS Sector 14 was supported by the National Institutes of Health, National Center for Research Resources under grant No. RR07707.

References

Anderson, M. J., Hansen, C. L. & Quake, S. R. (2006). *Proc. Natl Acad. Sci. USA*, **103**, 16746–16751.
Angeles, T. S., Hunsley, J. R. & Viola, R. E. (1992). *Biochemistry*, **31**, 799–805.
Blanco, J., Moore, R. A., Faehnle, C. R., Coe, D. M. & Viola, R. E. (2004). *Acta Cryst.* D**60**, 1388–1395.
Blanco, J., Moore, R. A., Faehnle, C. R. & Viola, R. E. (2004). *Acta Cryst.* D**60**, 1808–1815.
Blanco, J., Moore, R. A., Kalabeeswaran, V. & Viola, R. E. (2003). *Protein Sci.* **12**, 27–33.
Blanco, J., Moore, R. A. & Viola, R. E. (2003). *Proc. Natl Acad. Sci. USA*, **100**, 12613–12617.
Cardineau, G. A. & Curtiss, R. (1987). *J. Biol. Chem.* **262**, 3344–3353.
Carter, C. W. (1997). *Methods Enzymol.* **276**, 74–99.
Carter, C. W. Jr & Carter, C. W. (1979). *J. Biol. Chem.* **254**, 12219–12223.
Chayen, N. E. & Saridakis, E. (2002). *Acta Cryst.* D**58**, 921–927.
Cohen, G. N. (1983). *Amino Acids: Biosynthesis and Genetic Regulation*, edited by K. M. Herrmann & R. L. Somerville, pp. 147–171. Reading, USA: Addison–Wesley.
Collaborative Computational Project, Number 4 (1994). *Acta Cryst.* D**50**, 760–763.
Collins, B., Stevens, R. C. & Page, R. (2005). *Acta Cryst.* F**61**, 1035–1038.
Collins, B. K., Tomanicek, S. J., Lyamicheva, N., Kaiser, M. W. & Mueser, T. C. (2004). *Acta Cryst.* D**60**, 1674–1678.
Cox, R. J., Hadfield, A. T. & Mayo-Martin, M. B. (2001). *Chem. Commun.* **18**, 1710–1711.
Cudney, R., Patel, S., Weisgraber, K., Newhouse, Y. & McPherson, A. (1994). *Acta Cryst.* D**50**, 414–423.
Ellis, G. (2006). *Clin. Biochem.* **39**, 1035–1040.
Faehnle, C. R., Le Coq, J., Liu, X. & Viola, R. E. (2006). *J. Biol. Chem.* **281**, 31031–31040.
Faehnle, C. R., Liu, X., Pavlovsky, A. & Viola, R. E. (2006). *Acta Cryst.* F**62**, 962–966.
Faehnle, C. R., Ohren, J. F. & Viola, R. E. (2005). *J. Mol. Biol.* **353**, 1055–1068.
Faruque, S. M., Albert, M. J. & Mekalanos, J. J. (1998). *Microbiol. Mol. Biol. Rev.* **62**, 1301–1314.
Galan, J. E., Nakayama, K. & Curtiss, R. (1990). *Gene*, **94**, 29–35.
Gouet, P., Courcelle, E., Stuart, D. I. & Metoz, F. (1999). *Bioinformatics*, **15**, 305–308.
Hadfield, A. T., Kryger, G., Ouyang, J., Petsko, G. A., Ringe, D. & Viola, R. E. (1999). *J. Mol. Biol.* **289**, 991–1002.
Han, S., Moore, R. A. & Viola, R. E. (2003). *Synlett*, pp. 845–846.
Harb, O. S. & Kwaik, Y. A. (1998). *Infect. Immun.* **66**, 1898–1903.
Hayward, S. & Berendsen, H. J. C. (1998). *Proteins*, **30**, 144–154.
Hayward, S. & Lee, R. A. (2002). *J. Mol. Graph.* **21**, 181–183.
Izaac, A., Schall, C. A. & Mueser, T. C. (2006). *Acta Cryst.* D**62**, 833–842.
Jancarik, J. & Kim, S.-H. (1991). *J. Appl. Cryst.* **24**, 409–411.
Jancarik, J., Pufan, R., Hong, C., Kim, S.-H. & Kim, R. (2004). *Acta Cryst.* D**60**, 1670–1673.
Kantardjieff, K. & Rupp, B. (2004). *Bioinformatics*, **20**, 2162–2168.
Karsten, W. E. & Viola, R. E. (1991). *Biochim. Biophys. Acta*, **1077**, 209–219.
Karsten, W. E. & Viola, R. E. (1992). *Biochim. Biophys. Acta*, **1121**, 234–238.
Kimber, M. S., Vallee, F., Houston, S., Necakov, A., Skarina, T., Evdokimov, E., Beasley, S., Christendat, D., Savchenko, A., Arrowsmith, C. H., Vedadi, M., Gerstein, M. & Edwards, A. M. (2003). *Proteins*, **51**, 562–568.
Kish, M. M. & Viola, R. E. (1999). *Inorg. Chem.* **38**, 818–820.
Kryuk, T. V., Mikhal'chuk, V. M., Petrenko, L. V., Nelepova, O. A. & Nikolaevskii, A. N. (2002). *Pharm. Chem. J.* **36**, 32–35.
Laskowski, R. A., MacArthur, M. W., Moss, D. S. & Thornton, J. M. (1993). *J. Appl. Cryst.* **26**, 283–291.
Lassmann, T. & Sonnhammer, E. L. (2006). *Nucleic Acids Res.* **34**, W596–W599.
Lu, G. (1996). *Protein Data Bank Q. Newsl.* **78**, 10–11.
McCoy, A. J., Grosse-Kunstleve, R. W., Storoni, L. C. & Read, R. J. (2005). *Acta Cryst.* D**61**, 458–464.
Matthews, B. W. (1974). *J. Mol. Biol.* **82**, 513–526.
Moore, R. A., Bocik, W. E. & Viola, R. E. (2002). *Protein Expr. Purif.* **25**, 189–194.
Murshudov, G. N., Vagin, A. A. & Dodson, E. J. (1997). *Acta Cryst.* D**53**, 240–255.
Newman, J., Egan, D., Walter, T. S., Meged, R., Berry, I., Ben Jelloul, M., Sussman, J. L., Stuart, D. I. & Perrakis, A. (2005). *Acta Cryst.* D**61**, 1426–1431.
Nichols, C. E., Dhaliwal, B., Lockyer, M., Hawkins, A. R. & Stammers, D. K. (2004). *J. Mol. Biol.* **341**, 797–806.
Otwinowski, Z. & Minor, W. (1997). *Methods Enzymol.* **276**, 307–326.
Paidhungat, M., Setlow, B., Driks, A. & Setlow, P. (2000). *J. Bacteriol.* **182**, 5505–5512.
Pavelka, M. S. & Jacobs, W. R. (1996). *J. Bacteriol.* **178**, 6496–6507.
Schoolnik, G. K. & Yildiz, F. H. (2000). *Genome Biol.* **3**, 1016.1–1016.3.
Schubert, H. L., Raux, E., Warren, M. J. & Wilson, K. S. (2001). *Acta Cryst.* D**57**, 867–869.
Stura, E. A., Satterthwait, A. C., Calvo, J. C., Kaslow, D. C. & Wilson, I. A. (1994). *Acta Cryst.* D**50**, 448–455.
Tran, T. T., Sorel, I. & Lewit-Bentley, A. (2004). *Acta Cryst.* D**60**, 1562–1568.
Tsodikov, O. V., Record, M. T. & Sergeev, Y. V. (2002). *J. Comput. Chem.* **23**, 600–609.
Vagin, A. & Teplyakov, A. (1997). *J. Appl. Cryst.* **30**, 1022–1025.
Viola, R. E. (2001). *Acc. Chem. Res.* **34**, 339–349.